Supporting Information to

Alkali Doping Leads to Charge-Transfer Salt Formation in a Two-Dimensional Metal-Organic Framework

Phil J. Blowey[1,2♦], Billal Sohail[2♦], Luke A. Rochford[3], Timothy Lafosse[2], David A. Duncan[4], Paul T.P. Ryan[4,5], Daniel Andrew Warr[2], Tien-Lin Lee[4], Giovanni Costantini[2], Reinhard J. Maurer[2*], David Phillip Woodruff[1*]

[1]Department of Physics, University of Warwick, Coventry CV4 7AL, UK

[2]Department of Chemistry, University of Warwick, Coventry CV4 7AL, UK

[3]Chemistry Department, University of Birmingham, University Road, Birmingham B15 2TT, UK

[4]Diamond Light Source, Harwell Science and Innovation Campus, Didcot, OX11 0DE, UK

[5] Department of Materials, Imperial College, London SW7 2AZ, UK

Contents

1. Experimental Details, NIXSW data analysis and STM image simulation

The single crystal Ag(111) sample was cleaned *in situ* using cycles of sputtering with 1 keV Ar^+ ions for 30 minutes followed by annealing to ~500 °C for another 30 minutes. TCNQ powder (98% pure; Sigma Aldrich) was triply purified by thermal gradient sublimation and thoroughly degassed before being deposited onto the Ag(111) substrate from a Knudsen effusion cell at a nominal operating temperature

of 120 °C. K was deposited by resistive heating of a SAES dispenser source. STM images were recorded in constant current mode using electrochemically etched polycrystalline tungsten tips. All STM images were plane corrected and flattened using the open source image-processing software Gwyddion[1].

Synchrotron radiation X-ray photoelectron spectroscopy (SXPS) characterisation and normal incidence X-ray standing wave (NIXSW) measurements were performed in the UHV end-station installed on beamline I09 of the Diamond Light Source. This beamline is equipped with both a crystal monochromator to provide the 'hard' X-rays needed to perform the NIXSW experiments and a grazing incidence plane grating monochromator delivering soft X-rays to perform high-resolution SXPS. Both the SXP spectra and the higher photon energy XP spectra used in the NIXSW measurements were recorded using a VG Scienta EW4000 HAXPES hemispherical electron analyser mounted at 90° to the incident photon beam, while sweeping the photon energy through the (111) Bragg condition at near-normal incidence to the surface. The high-resolution SXP spectra and the XP spectra recorded in NIXSW experiments were fitted using the CasaXPS software package. Table S1 shows a comparison of the photoelectron core level binding energies derived from the SXP spectra of the K_2TCNQ overlayer and the Ag-TCNQ surface layer.

Table S1. Photoelectron binding energies in eV of the atomic components for TCNQ adsorbed in the commensurate (Ag-adatom-containing) phase on Ag(111)[2] and from the commensurate K_2TCNQ coadsorption phase.

Component	**CH**	**CC_1**	**CC_2**	**CN**	**K $2p_{3/2}$**	**K $2p_{1/2}$**	**N**
Ag(111)-K_2TCNQ	284.0	284.5	284.8	285.6	293.3	296.1	398.1
Ag(111)-Ag-TCNQ	283.8	284.3	284.7	285.4	-	-	398.0

The NIXSW technique[3] exploits the X-ray standing wave formed by the interference of incident and scattered X-rays at a Bragg condition. The strong

backscattering out of the crystal leads to a finite extinction depth of the X-rays, resulting in high reflectivity over a finite range of incident X-ray energies. Within this range the standing wave, which has a periodicity in intensity equal to that of the scattering planes, shifts in phase relative to the scattering planes in a systematic fashion. Monitoring the X-ray absorption at atoms immersed in the standing wave (within or above the crystal) through this photon energy range thus provides a profile characteristic of the height of the absorbing atoms above the scattering planes. The use of photoemission to monitor the absorption allows one to exploit the element and chemical-state-specific photoelectron binding energies in order to extract structural data from each locally inequivalent atom in the overlayer. The measured NIXSW absorption profiles can by uniquely fitted by two structural parameters, the coherent fraction, *f*, and the coherent position, *p*. The coherent fraction is commonly regarded as an order parameter, with a value of unity for a single adsorption geometry that is perfectly (statically and dynamically) ordered. Typically, values of ~0.8 or larger for this parameter are regarded as indicative of occupation of a well-defined single site, in which case the coherent position gives the height of this site, relative to the atomic scattering planes of the Bragg reflection, in units of the spacing of these scatterer planes. In the present case, using normal incidence to the surface and the (111) Bragg condition, this is the height of the absorbing atom above the surface, referenced to the nearest extended scattering plane. Much lower values of *f* may be indicative of two or more contributing heights, the measured coherent position being some weighted average of these different values. The coherent position *p* can be converted to a height using the conversion formula $D=(n+1)d_{(111)}$, where $d_{(111)}$ is the Ag(111) bulk interlayer spacing and *n* is an integer, chosen to ensure that interatomic bond lengths between the substrate and the molecule fall in a physically reasonable range.

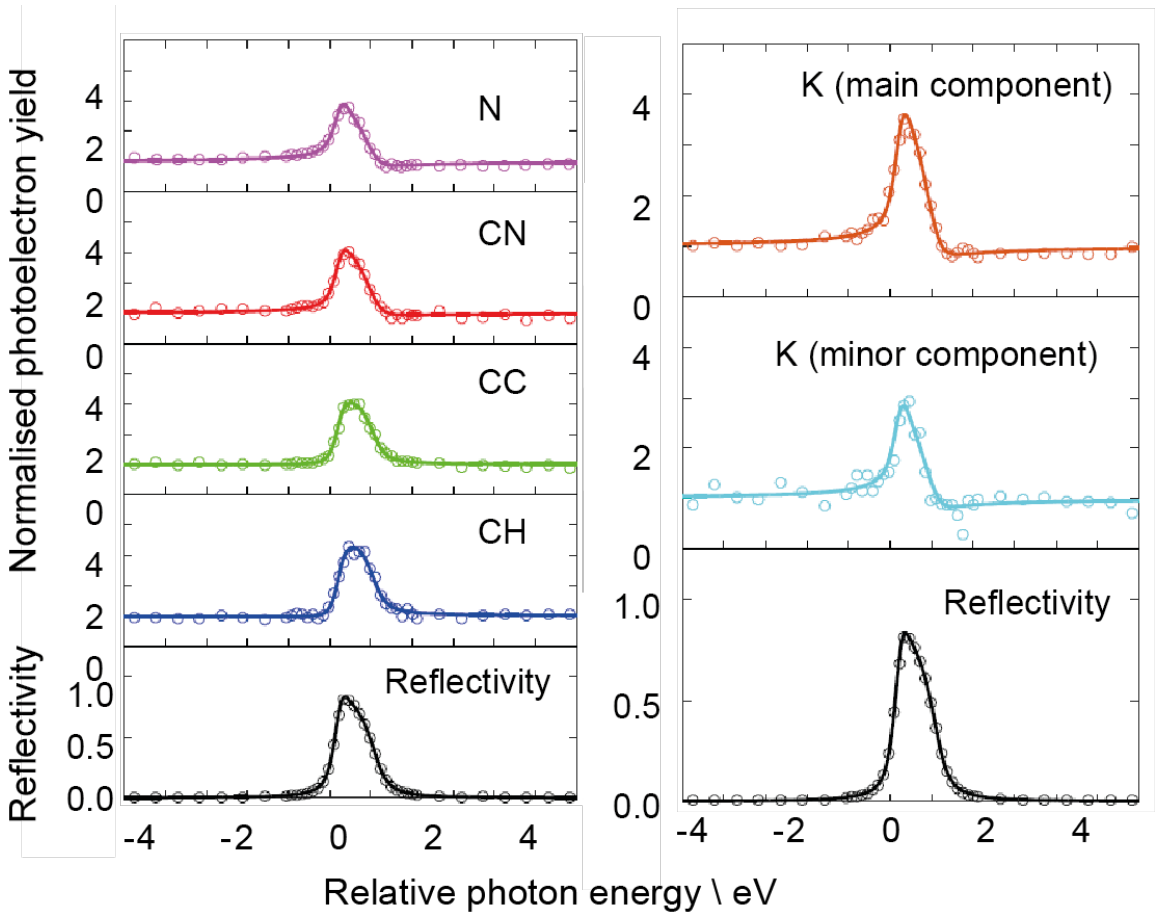

Figure S1 (111) NIXSW photoemission yield curves and reflectivity measurements for K_2TCNQ on Ag(111). The solid lines are least-squared fits to the experimental data (circles). The photon energy is give relative to the Bragg energy of 2630 eV.

Figure S1 shows the raw NIXSW data obtained from the Ag(111)-K_2TCNQ surface, while Table S2 summarises the NIXSW structural parameters extracted from these measurements and compares them with the values previously reported[2] for the Ag-TCNQ overlayer in the commensurate phase, including the coherent fraction values.

Table S2 Comparison of the NIXSW structural parameters for the commensurate (Ag-adatom-containing) overlayer of TCNQ on Ag(111)[2] and the commensurate coadsorption phase K_2TCNQ on Ag(111). Precision estimates, in units of 0.01, are shown in parentheses. The poor precision estimates for the coherent fractions take account of the problems of photoelectron detector non-linearity discussed in more detail previously.[4]

	f		*D* /Å	
Component	Ag-TCNQ	K_2TCNQ	Ag-TCNQ	K_2TCNQ
CH	0.95(10)	0.86(10	2.86(5)	2.97(5)
CC	0.99(10)	0.66(10)	2.78(5)	2.99(5)
CN	0.89(10)	0.56(10	2.76(5)	3.22(5)
N	0.39(10)	0.55(10)	2.75(5)	3.30(5)
K (main)	-	0.81(10)	-	3.29(7)
K (minor)	-	0.47(10)	-	3.65(16)

The results for the K_2TCNQ commensurate overlayer show a coherent fraction for the C atoms bonded only to H atoms ('CH') that is sufficiently high to be indicative of a single contributing height, but the values for the other C atoms are significantly lower. Notice, though, that the lowest values for *f* correspond to those C atoms with the largest difference in *D* between the TCNQ and K_2TCNQ coadsorption phase. One possible reason for the reduced *f* values for these C atoms could therefore be that there are some pure TCNQ regions coexisting with the majority K_2TCNQ phase areas on the surface. Coexisting areas of the incommensurate KTCNQ phase[4] would have the same effect, as the *D* values for this phase are very similar to those of the pure TCNQ phase. If this were to be the reason for the reduced *f* values, the true heights of the CC and CN atoms in the K_2TCNQ phase may be a few hundredths of an ångström larger than the values reported in Table S2. A similar effect could account for the *f* value of the N atoms, which is the same as that of the C atoms ('CN') bonded to N; notice that the atomic height difference between the pure TCNQ and coadsorption phases are largest for the CN and N

atoms, so some admixture of the two phases would lower these measured *f* values the most.

The very low *f* value for N in the Ag-TCNQ phase has been shown to be due to two distinctly different N heights in a twisted molecule, arising from the presence of the Ag adatoms in the overlayer structure;[2] in the K_2TCNQ phase this parameter is not so anomalously low. The high *f* value for the main K peak, and the much lower value for the minor K component, are fully consistent with the suggestion in the main text that the main peak corresponds to K atoms at a single well-defined height in the 2D-MOF, while the minor K component is related to excess K atoms that may lie above the 2D-MOF (possibly at a height 2.35 Å higher than the value reported in the table, with a *n* value of 2 rather the value of 1 used in the table), or in other disordered regions of the surface

Predicted values for the coherent fractions for the K_2TCNQ phase obtained from the different DFT calculations are shown in Table S3. These calculations take no account of the dynamic and static disorder of the experiment (including possible partial coexistence of two surface phases) and are thus all higher than the experimental values.

The predicted values of the coherent positions are given in the main manuscript in Table 2. Notice that in the NIXSW technique coherent positions are determined relative to the locations of the (extended) atomic planes on the bulk of the substrate. In a DFT calculation based on a thin metallic slab there is no true ‘bulk. Moreover, the computed lattice parameter, and thus also the bulk interlayer spacing, differ slightly from the experimental values. In addition, while fcc metal (111) surfaces are known to show extremely small surface relaxations, this is not always true of DFT slab calculations. In fact the surface relaxation predicted by the PBE+vdW^{surf} calculations is negligible (approx. 0.01 Å), but the PBE+MBD calculations predict a much stronger, artificial relaxation. To overcome these problems the reported coherent positions derived from the DFT calculations are of

the adlayer atom heights relative to average height of the outermost (slightly rumpled) Ag atom layer.

Table S3 Coherent fraction values for the K_2TCNQ phase according to the different DFT calculations described in the text.

f	CH	CC	CN	N	K
Experiment	0.86	0.66	0.56	0.55	0.81
vdW^{Surf}	1.00	0.99	0.93	0.75	1.00
MBD	1.00	0.99	0.99	0.95	1.00
$vdW^{Surf}(K^+)$	1.00	0.99	1.00	1.00	1.00
$MBD(K^+)$	1.00	0.98	1.00	1.00	1.00

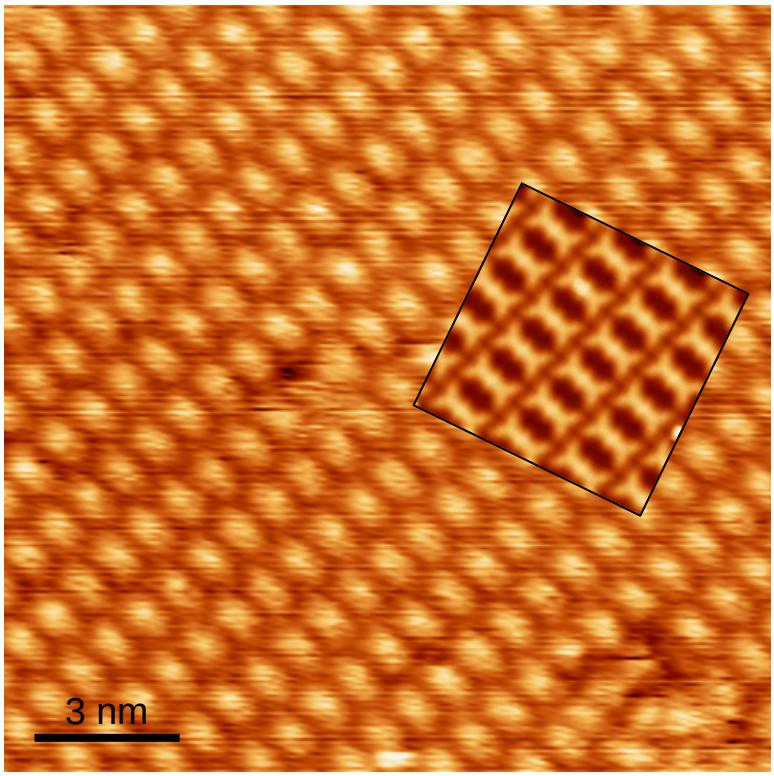

Figure S2 Simulated STM image of the K_2TCNQ surface, shown in the square box, overlaid on a section of the experimental image taken from Fig. 1(a) of the main paper.

In order to try to gain a better understanding of why the STM images of Fig. 1 of the main paper fail to show any features attributable to the locations of the K atoms in the K_2TCNQ phase we have calculated simulated images from our DFT calculations using the Tersoff-Hamman[5] approach. The results is shown in Fig. S2 overlaid on a section of the experimental image of Fig. 1(a). Simulated images using this technique invariably show higher spatial resolution than is found in experimental STM images, even when formed using very low isosurface values – the simulation shown is based on an isovalue of 0.005 – and including Gaussian blurring of 3 Å to take some account of the effects of finite tip size, external vibrational noise and molecule movement (to be expected for the room temperature experimental imaging). Weak features due to the K atoms could only be seen in simulated images at much higher isovalues corresponding to the very short tip-surface separations used in STM-derived scanning probe techniques, such as scanning tunnelling hydrogen microscopy (STHM)[6] or bond-resolved scanning tunnelling microscopy (BRSTM)[7] .

2. Computational Details of Density Functional Theory calculations

The theoretical analysis has been performed at the density functional theory (DFT) level using the Fritz-Haber institute *ab* initio molecular simulations package (FHI-aims) [8]. The adsorption of aromatic molecules on metal surfaces poses a great theoretical challenge as it depends upon careful characterisation of van der Waals (vdW) forces, which are heavily influenced by geometric and structural orientation of the molecule on the surface. Long-range vdW forces are missing in most commonly employed density functional approximations based on the generalised gradient approximation (GGA). To address this issue, we employed the GGA functional defined by Perdew, Burke and Ernzerhofer (PBE)[9] with two different long-range dispersion corrections: Tkatchenko-Scheffler van der Waals correction for metal surfaces (vdW^{surf}) [10] and many-body dispersion correction (MBD).[11, 12] Structural models were created using the atomic simulation environment (ASE)[13]. The structural model investigated was based on lateral periodicity as determined by STM and LEED, while STM images provided an initial indication of the number

and relative orientation of TCNQ molecules within the unit mesh, and SXPS gave an estimate of the stoichiometry. To model the K_2TCNQ overlayer on Ag(111) we employed 4 layers of metal with a $\begin{pmatrix} 3 & 0 \\ 1 & 5 \end{pmatrix}$ unit mesh. The surface lattice parameter was set to the PBE value for bulk Ag of 4.14 Å. To optimise the structures, the BFGS algorithm[14] was employed with a force criterion of 0.025 eV/Å. The bottom 2 layers of the metal slab were constrained to the bulk truncated structure, allowing the upper 2 layers and the adsorbate to relax. In the case of PBE+vdW^{surf}, we exclude vdW interactions between Ag atoms. FHI-aims contains built-in basis set settings of each atomic species regarding basis functions, integration grid and numerical accuracy of the Hartree potential. All equilibrium structures were optimised with the default "tight" basis set, which was determined to be sufficient to establish converged interaction energies and equilibrium structures. A vacuum slab of 32 Å in the z coordinate was used for all calculations. To characterise the potassium atoms within the coadsorbed system we employed rescaled C_6, polarisation and van der Waals radius coefficients (see section 3 below for details). The initial structure of the Ag-TCNQ system was taken from Blowey *et al.*,[2] then reoptimised with PBE+vdW^{surf}.

Following optimisation calculations, single-point calculations were performed with a k-grid of 4×4×1(with other selected calculations being computed with a k-grid of 8×8×1). Single point calculations included examination of stabilisation/interaction energies, Hirshfeld charge partitioning analysis, molecular orbital projected density of states (MODOS) and density difference calculations. Iterative Hirshfeld and Hirshfeld charge partitioning calculations were performed using the “tight” basis set functions however, the numerical integration grid was replaced with the “really tight” settings. This was necessary to reduce integration errors in the calculation of atomic net charges in both methods.

3. Details of dispersion parameter rescaling for potassium

Within this work we employed two distinct dispersion correction schemes, vdW^{surf} and MBD. Both of these schemes use atomic reference values for atomic polarisability, C6 coefficient and van der Waals (vdW) radius for neutral free atoms as input data. These tabulated parameters are then rescaled based on the ratio between the effective atoms-in-molecules (AIM) volume and the free atom volume:

$$\alpha_K^{AIM} = \left(\frac{V^{\text{eff}}}{V^{\text{neutral.free}}}\right) \alpha_K^{\text{free}} \qquad \text{S1}$$

This scheme is known to underestimate the effect of strong charge transfer in polar chemical bonding situations. To better describe long-range dispersion interactions involving K^+, we replace the free atom reference polarizability of neutral K with the one for K^+ and we add a scaling pre-factor to change the reference volume:

$$\alpha_{K^+}^{AIM} = \left(\frac{V^{\text{neutral.free}}}{V^{+1.\text{free}}}\right) \alpha_{K^+}^{\text{free}} \left(\frac{V^{\text{eff}}}{V^{\text{neutral.free}}}\right) \qquad \text{S2}$$

Equation S2 was used within our locally modified FHI-aims package to calculate polarisability. The static polarisability of K^+ is taken from Gould *et al*. [15]

4. Charge analysis data for K_2-TCNQ and Ag-TCNQ on Ag(111)

Table S4 Iterative and non-iterative Hirshfeld charge values for all species in the K_2TCNQ unit cell. Units in elementary electronic charge *e*.

K_2TCNQ	K (per atom)[†]	TCNQ (per molecule)	Total substrate charge (per surface unit mesh)
Iterative Hirshfeld	1.058	-2.033	-0.083
Hirshfeld	0.304	-0.971	0.363

[†] Two K atoms in the unit cell.

Table S5 Iterative and non-iterative Hirshfeld charge values for all species in the Ag-TCNQ unit cell. Units in elementary electronic charge *e*.

Ag-TCNQ	Ag adatoms (per atom)‡	TCNQ (per molecule)	Total substrate charge (per surface unit mesh)
Iterative Hirshfeld	0.434	-1.169	2.205
Hirshfeld	0.240	-0.780	1.620

Table S6 Iterative and non-iterative Hirshfeld charge values for all spectroscopic species in the K_2TCNQ unit cell. Units in elementary electronic charge *e*.

K_2TCNQ	K (per atom)	CH (per atom)	CN (per atom)	CC (per atom)	N (per atom)
Iterative Hirshfeld	1.058	-0.196	-0.458	-0.190	-0.705
Hirshfeld	0.304	-0.063	-0.070	-0.042	-0.237

Table S7 Iterative and non-iterative Hirshfeld charges for all spectroscopic species in the Ag-TCNQ unit cell. Units in elementary electronic charge *e*.

Ag-TCNQ	Ag Adatoms (per atom)	CH (per atom)	CN (per atom)	CC (per atom)	N (per atom)
Iterative Hirshfeld	0.434	-0.194	0.420	-0.163	-0.485
Hirshfeld	0.240	-0.029	-0.070	-0.037	-0.198

‡ Three Ag adatoms per unit cell.

5. Calculation of energy level diagrams of K_2TCNQ and Ag-TCNQ on Ag(111)

Molecular orbital projected density of states (MODOS) provide a method of projecting gas phase molecular orbitals onto the electronic structure of a metal-organic interface. The density of states (DOS) of a quantum mechanical system as a function of energy is defined as,

$$\rho(E) = \sum_i \langle \phi_i | \phi_i \rangle \delta(E - \epsilon_i) \qquad \text{S3}$$

where, ϕ_i is an energy eigenstate of the system and ϵ_i is the corresponding energy eigenvalue. The utility of such a method allows a projection onto a complete orthogonal basis set $\{\zeta_\mu(r)\}$ without loss of information.

$$\rho(E) = \sum_\mu \sum_i \langle \phi_i | \zeta_\mu \rangle \langle \zeta_\mu | \phi_i \rangle \delta(E - \epsilon_i) = \sum_\mu \sum_i \left| \langle \zeta_\mu | \phi_i \rangle \right|^2 \delta(E - \epsilon_i) = \sum_\mu \rho_\mu(E) \qquad \text{S4}$$

If the single state $\zeta_\mu(r)$ belongs to one of the molecular orbitals (MOs) of a molecule in the gas phase, this gives an MO-projected DOS or MODOS.

The results are shown in figure 6 of the main manuscript.

Equation S5 defines the methodology to obtain energy level peak positions for an adsorbed molecule as presented in figure 5 of the main manuscript. The energy level position E_μ is obtained by integration over the energy weighted by the MODOS of the corresponding frontier orbital $\rho_\mu(E)$,[12]

$$E_\mu = \frac{\int E \cdot \rho_\mu(E) dE}{\int \rho_\mu(E) dE} \qquad \text{S5}$$

6. Ultraviolet photoemission from the valence states and measured work functions

UP spectra using conventional He I ($h\nu$ = 21.22 eV) radiation are shown in Figure S3(b) while Figure S3(a) shows the measurements of the secondary electron cut-off of UP spectra with an applied sample bias of −10 V in order to determine the work function. The values obtained are reported in the main text.

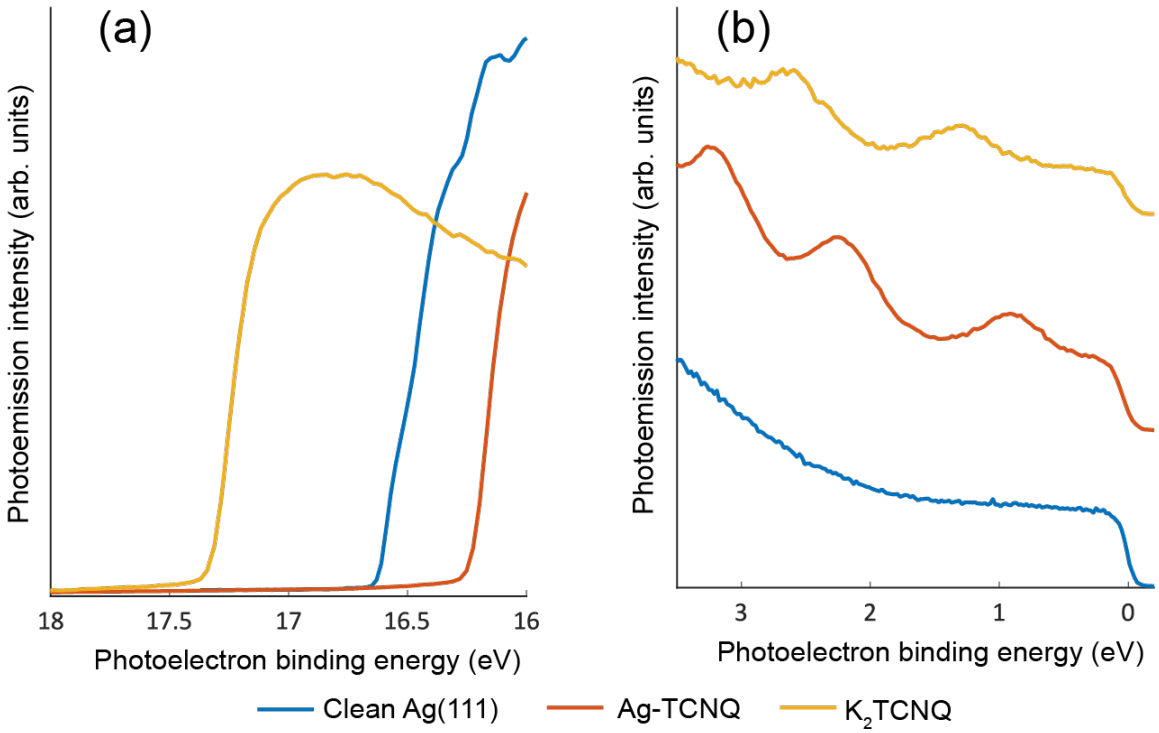

Figure S3 UP spectra obtained with (a) a sample bias of −10 V to show the secondary electron cut-off and (b) with no applied bias to show emission from the shallowly bound molecular orbital states.

7. Calculation of work function on K_2TCNQ and Ag-TCNQ on Ag(111)

Table S8 - Work functions computed for both adsorbate systems and the clean surface. Reported are the work function ϕ, the respective change in work function when compared to the clean substrate Δϕ, the electrostatic contribution of the work function change from the adsorbate overlayer ΔE_{mol}, and the contribution of the work function change due to the chemical interaction of the overlayer with the metal ΔE_{bond}. The two contributions sum up to the total work function change: $\Delta\phi = \Delta E_{mol} + \Delta E_{bond}$

	Work function ϕ / eV	$\Delta\phi$ / eV	ΔE_{mol} / eV	ΔE_{bond} / eV
Ag(111)	4.43			
K_2TCNQ/Ag(111)	4.11	-0.31	-0.69	0.38
Ag-TCNQ/Ag(111)	4.90	0.47	-0.02	0.49

Table S8 provides a breakdown of work function values for the total system, the pristine metal surface and the difference between the adsorbate-substrate system

and the pristine substrate work function, respectively. We can decompose the change in work function for both systems into contributions from the electrostatic dipole moment of the overlayer (ΔE_{mol}) and from the bond between the metal and the overlayer ($\Delta \mathrm{E}_{\mathrm{bond}}$). We find that the bond contribution is slightly larger for the Ag-TCNQ case, but the dominant difference between the two is the large electrostatic potential drop introduced by the dipole density of the K_2TCNQ salt layer.

8. Density difference plots of K_2TCNQ and Ag-TCNQ on Ag(111)

Density difference contour plots ($\Delta\rho$) were calculated using equation S6 for K_2TCNQ and Ag-TCNQ in order to understand and visibly elucidate the charge re-arrangement of the atoms and molecules upon adsorption.

$$\Delta\rho = \rho(\mathrm{Total\ System}) - [\rho(\mathrm{Ag/K}) + \rho(\mathrm{TCNQ}) + \rho(\mathrm{Ag}_{111})] \qquad \text{S6}$$

Figures S4 and S5 depict the density difference due to the interaction of all the interface constituents for K_2TCNQ and Ag-TCNQ. Blue areas indicate loss of electrons (positive net charge), red areas indicate accumulation of electrons (negative net charge). Figures S4(a) and S5(a) depict integrated charge density differences perpendicular to the surface. The Ag-TCNQ system shows a much stronger charge separation and density change between adlayer and substrate due to the adsorption than K_2TCNQ. This is consistent with the larger net charge transfer. Subplots (c) to (e) in Figures S4 and S5 show x-y cuts parallel to the surface through the density difference at various heights. Here it is evident that K_2TCNQ experiences stronger charge separation within the adlayer (x-y) plane than Ag-TCNQ. In both cases, the charge accumulation/depletion in the TCNQ molecule clearly corresponds to charge flow into the LUMO orbital of the isolated TCNQ molecule, mostly *via* charge accumulation at the terminal C-N groups.

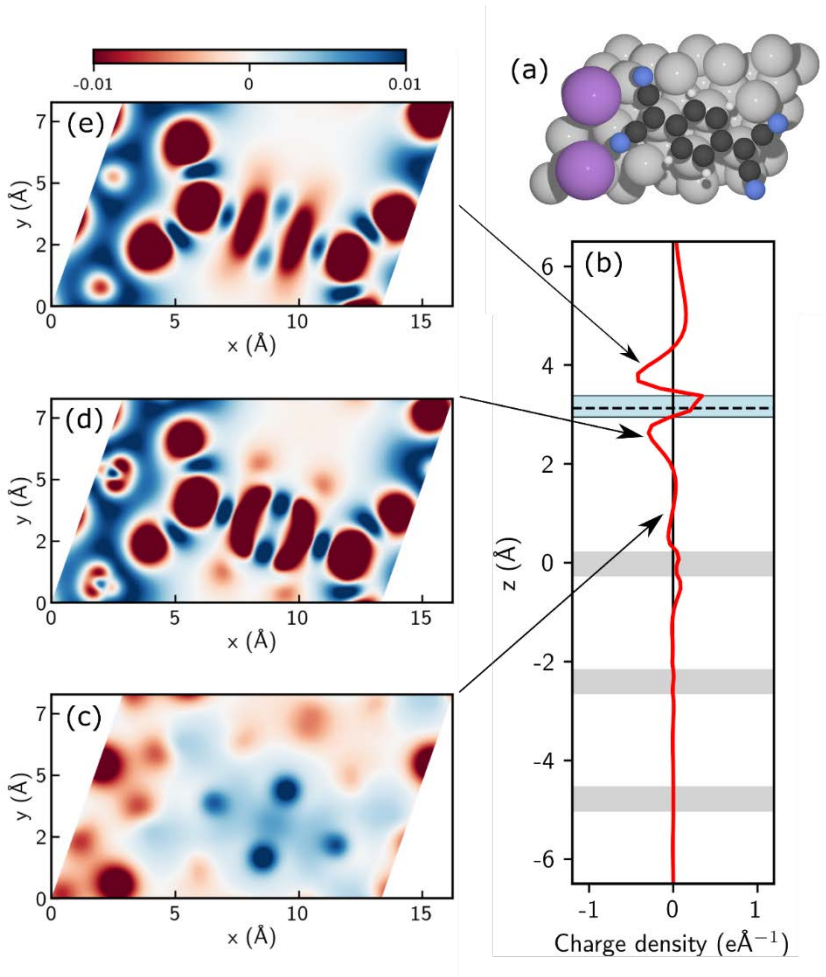

Figure S4 – (a) top view of K_2TCNQ on Ag(111). (b) Charge density difference after integrating in x and y directions parallel to the surface. The grey horizontal bars indicate the position of the substrate layers. The dashed black horizontal line locates the centre of mass of the adsorbed molecule and the blue region in (b) shows the minimum and maximum heights, z, of the atoms in the adlayer. (c)-(e) Charge density difference for x-y plane cuts parallel to the surface through the system at 1.0 Å (c), 2.60 Å (d), and 4.0 Å (e) distance from the average 1st substrate layer. Red areas correspond to negative charge accumulation; blue areas correspond to positive charge accumulation with respect to the isolated reference systems. Units in elemental charge per unit volume ($e \cdot \AA^{-3}$).

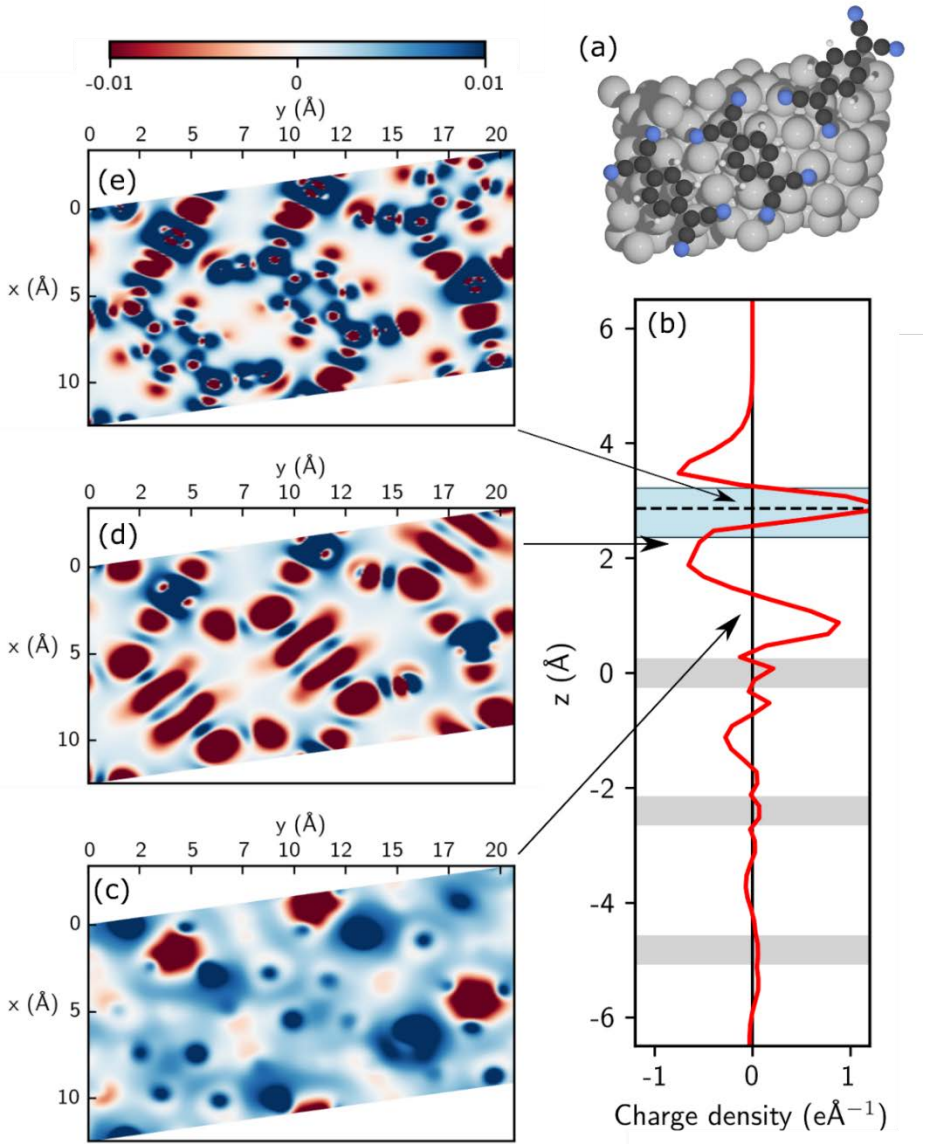

Figure S5 a) top view of Ag-TCNQ on Ag(111). (b) Charge density difference after integrating in x and y direction parallel to the surface. The grey horizontal bars indicate the position of the substrate layers. The dashed black horizontal line locates the centre of mass of the adsorbed molecule and the blue region in (b) shows the minimum and maximum heights, z, of the atoms in the adlayer. (c)-(e) Charge density difference for x-y plane cuts parallel to the surface through the system at 1.0 Å (c), 2.20 Å (d), and 2.80 Å (e) distance from the average 1st substrate layer. Red areas correspond to negative charge accumulation; blue areas correspond to positive charge accumulation with respect to the isolated reference systems. Units in elemental charge per unit volume ($e \cdot \AA^{-3}$).

AUTHOR INFORMATION

Corresponding authors

*E-mail: d.p.woodruff@warwick.ac.uk
*E-mail: r.maurer@warwick.ac.uk

Author contributions

♦P.J. Blowey and S. Billal contributed equally

---

1 D. Nečas and P. Klapetek, Gwyddion: an Open-Source Software for SPM Data Analysis, *Cent. Eur. J. Phys.*, **2012**, *10*, 181-188.

2 P.J. Blowey, S. Velari, L.A. Rochford, D.A. Duncan, D.A. Warr, T.-L. Lee, A. De Vita, G. Costantini, D.P. Woodruff, Re-Evaluating How Charge Transfer Modifies the Conformation of Adsorbed Molecules, *Nanoscale*, **2018**, *10*, 14984-14992.

3 D. P. Woodruff, Surface Structure Determination Using X-Ray Standing Waves, *Rep. Prog. Phys.*, **2005**, *68*, 743-798.

4 P. J. Blowey, L. A. Rochford, D. A. Duncan, D. A. Warr, T.-L. Lee, D.P. Woodruff, and G. Costantini, Probing the Interplay Between Geometric and Electronic Structure in a Two-Dimensional K-TCNQ Charge Transfer Network, *Faraday Disc.*, **2017**, *204*, 97-110.

5 J. Tersoff and D. R. Hamann, Theory of the Scanning Tunneling Microscope, *Phys. Rev. B*, **1985**, *31*, 805-813.

6 R. Temirov, S. Soubatch, O. Neucheva, A.C. Lassise and F.S. Tautz, A Novel Method of Achieving Ultra-High Geometrical Resolution in Scanning Tunnelling Microscopy, *New J. Phys*. **2008**, *10*, 053012.

7 G.D. Nguyen, H.-Z. Tsai, A.A. Omrani, T. Marangoni, M. Wu., D.J. Rizzo, G.F. Rodgers, R.R. Cloke, R.A. Durr, Y. Sakai, F. Liou, A.S. Aikawa, J.R. Chelikowsky, S.G. Louie, F.R. Fischer, and M.F. Crommie. Atomically Precise Graphene Nanoribbon Heterojunctions from a Single Molecular Precursor, *Nat. Nanotech*. **2017**, *12*, 1077.

8 V. Blum, R. Gehrke, F. Hanke, P. Havu, V. Havu, X. Ren, K. Reuter and M. Scheffler, *An Initio* Molecular Simulations with Numeric Atom-Centered Orbitals, *Comput. Phys. Commun.*, **2009**, *180*, 2175-2196.

9 J. P. Perdew, K. Burke and M. Ernzerhof, Generalised Gradient Approximation Made Simple, *Phys. Rev. Lett.*, **1996**, *77*, 3865-3868.

10 V. G. Ruiz, W. Liu, E. Zojer, M. Scheffler and A. Tkatchenko, Density-Functional Theory with Screened van der Waals Interactions for the Modelling of Hybrid Inorganic-Organic Systems, *Phys. Rev. Lett.*, **2012**, *108*, 146103.

11 A. Tkatchenko, R. A. DiStasio, R. Car and M. Scheffler, Accurate and Efficient Method for Many-Body van der Waals Interactions, *Phys. Rev. Lett.*, **2012**, *108*, 236402.

12 R. A. DiStasio, Jr., V. V. Gobre and A. Tkatchenko, Many-Body van der Waals Interactions in Molecules and Condensed Matter, *J. Phys.: Condens. Matter*, **2014**, *26*, 213202.

13 A. H. Larsen, J. J. Mortensen, J. Blomqvist, I. E. Castelli, R. Christensen, M. Dułak, J. Friis, M. N. Groves, B. Hammer, C. Hargus, E.D. Hermes, P.C. Jennings, P.B. Jensen, J. Kermode, J.R. Kitchin, E.L. Kolsbjerg, J. Kubal, K. Kaasbjerg, S. Lysgaard, J.N. Maronsson, *et al*., The Atomic Simulation Environment – A Python Library for Working with Atoms, *J. Phys.: Condens. Matter*, **2017**, *29*, 273002.

14 Jorge Nocedal and Stephen J. Wright. *Numerical Optimization*. 2nd. edition, Springer Science + Business Media, New York, USA, 2006, pp136-144.

15 T. Gould and T. Bučko, C-6 Coefficients and Dipole Polarizabilities for All Atoms and Many Ions in Rows 1-6 of the Periodic Table, *J. Chem. Theory Comput.*, **2016**, *12*, 3603-3613.